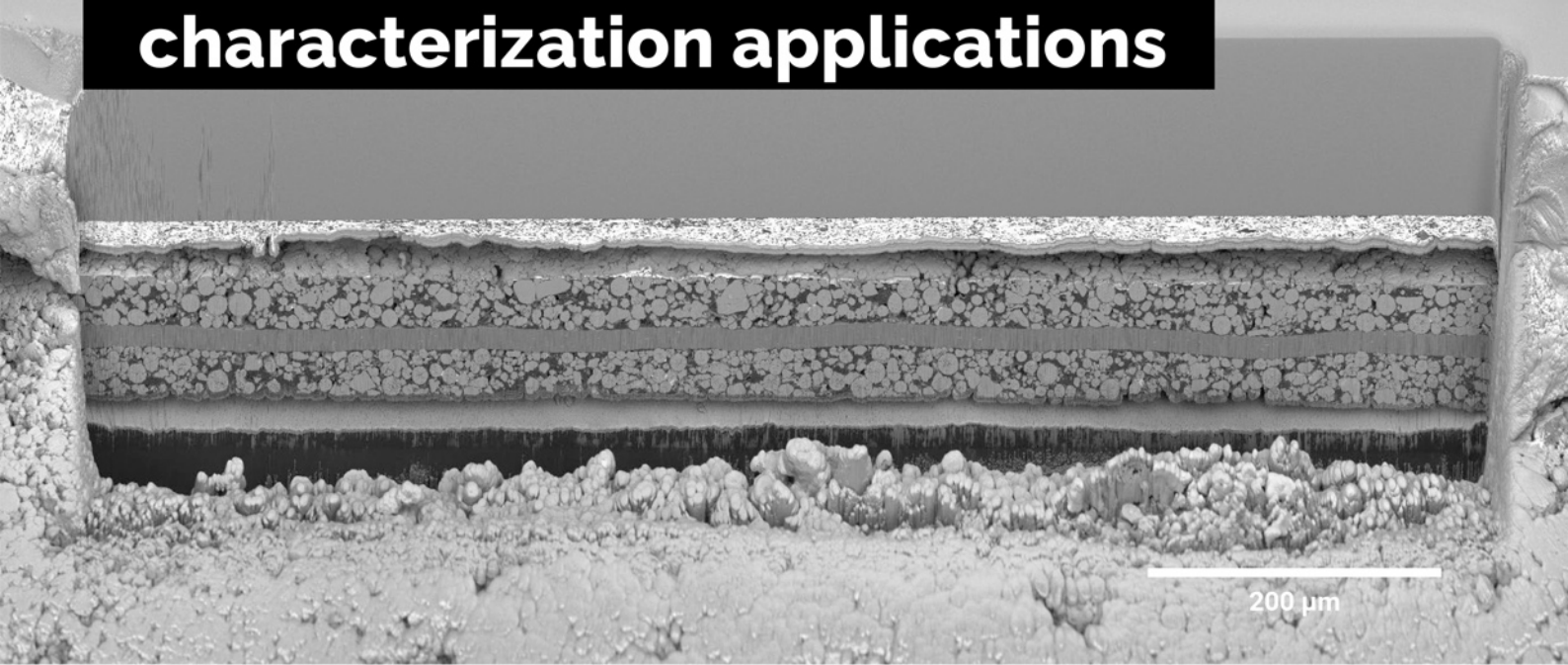


# A unique combination of Plasma FIB and field-free UHR SEM for the widest range of multiscale materials characterization applications



1 mm cross-section through a Li-ion battery electrode

## TESCAN AMBER X

- ✓ High throughput, large area FIB milling up to 1 mm
- ✓ Ga-free microsample preparation
- ✓ Ultra-high resolution, field-free FE-SEM imaging and analysis
- ✓ In-column SE and BSE detection
- ✓ Spot optimization for high-throughput, multi-modal FIB-SEM tomography
- ✓ Superior field of view for easy navigation
- ✓ Essence™ easy-to-use, modular graphical user interface



For more information visit

[www.tescan.com](http://www.tescan.com)

# Trimetallic Sulfide Mesoporous Nanospheres as Superior Electrocatalysts for Rechargeable Zn–Air Batteries

Haozhou Yang, Bin Wang, Haoyi Li, Bing Ni, Kai Wang, Qiang Zhang, and Xun Wang\*

Highly active and durable electrocatalysts are of great significance to accelerate the sluggish oxygen evolution and oxygen reduction reaction (OER and ORR) which are indispensable processes in practical devices such as metal–air batteries. Herein, the authors integrate morphological design with compositional manipulation, and successfully achieve well-defined CoNiFe sulfide mesoporous nanospheres (CoNiFe-S MNs). The as-prepared CoNiFe-S MNs exhibit superior OER and ORR catalytic activity, delivering a low overpotential of only 199 mV at a current density of 10 mA cm<sup>-2</sup> in 1 M KOH solution and a half-wave potential of 0.78 V in 0.1 M KOH solution toward OER and ORR, respectively. The CoNiFe-S MNs involved Zn–air battery exhibits remarkable charge–discharge performance (voltage gap of 0.76 V at 2 mA cm<sup>-2</sup>) and high power density (over 140 mW cm<sup>-3</sup>). Extended-time durability tests validate the structural recoverability of the mesoporous morphology, and the remarkable performance can be attributed to the intrinsic synergistic effect of heterometallic ions. It is believed that the method could pave the way for the design of novel electrocatalysts for Zn–air batteries.

processes, oxygen evolution reaction (OER) and oxygen reduction reaction (ORR). However, these two reactions extremely impede the overall efficiency due to their sluggish kinetics of four electron transfer.<sup>[4]</sup> Thus it is essential to develop high-performance electrocatalysts. Up to now, Pt-based materials and IrO<sub>2</sub> are regarded as state-of-the-art ORR and OER catalysts, respectively. Nevertheless, their high costs and poor stability greatly hinder the practical and large-scale applications.<sup>[5]</sup> Therefore, the rational design and accessible synthesis of low-cost and earth-abundant electrocatalysts with bifunctional activity are urgently needed.<sup>[6]</sup> A high-performance electrocatalysts should mainly meet the following three requirements.<sup>[7]</sup> First is the enhanced activity of exposed active sites in electrocatalysts, second is the improved intrinsic catalytic activity, and the third is the robust structural

stability which facilitate the mass transport. Accordingly, we found that the morphological and compositional manipulation are both essential to reach the demand of high electrocatalysts.

From the view of morphological design, mesoporous materials are promising candidates for highly desirable electrocatalysts.<sup>[8]</sup> The high porosity and large surface area are favorable for exposure of catalytic active sites and will benefit the mass transport and gas permeability.<sup>[9]</sup> Nonetheless, rather than diverse applications of mesoporous materials in solar cells, fuel cells, lithium batteries, and supercapacitors,<sup>[10]</sup> those in OER and ORR catalysis are overshadowed. Thus, it remains fascinating opportunities to combine the advantages of mesoporous materials with the demands of electrocatalysis.


From the perspective of compositional design, a large quantity of transition-metal-based novel catalysts, especially Fe, Co, Ni-contained oxides, hydroxides, chalcogenides, and phosphides have been extensively studied since their low costs and high catalytic performances meet the requirements of high-efficiency electrocatalysts.<sup>[11]</sup> Among them, Fe, Co, Ni-based sulfides have been proved high OER and ORR catalytic activity due to their rich catalytic active sites, good stability, and high electrical conductivity.<sup>[12–15]</sup> However, considering their broad applications in hydrogen evolution reaction,<sup>[16]</sup> researches on sulfide-based OER/ORR catalysts are still insufficient. Furthermore, the multimetal introduction is still insufficient. Therefore, fine modulation and preparation of novel-structured Fe, Co, Ni-based sulfides with high OER activity and durability

## 1. Introduction

The mounting pressure of resources and issues of environment have prompted great efforts to accelerate the development of conversion and storage related technologies for alternative energies.<sup>[1]</sup> Among them, metal–air batteries, especially Zn–air batteries, has been demonstrated promising candidate due to low cost and environmental benignity.<sup>[2]</sup> More importantly, The aqueous Zn–air battery has a theoretical energy density of 1086 W h kg<sup>-1</sup>, which is about five times higher than that of lithium ion batteries.<sup>[3]</sup> The charge and discharge of Zn–air batteries largely depend on two crucial electrochemical

H. Yang, H. Li, B. Ni, Dr. K. Wang, Prof. X. Wang  
Key Lab of Organic Optoelectronics and Molecular Engineering  
Department of Chemistry  
Tsinghua University  
Beijing 100084, China  
E-mail: wangxun@mail.tsinghua.edu.cn

Dr. B. Wang, Prof. Q. Zhang  
Beijing Key Laboratory of Green Chemical Reaction Engineering  
and Technology  
Department of Chemical Engineering  
Tsinghua University  
Beijing 100084, China

 The ORCID identification number(s) for the author(s) of this article can be found under <https://doi.org/10.1002/aenm.201801839>.

DOI: 10.1002/aenm.201801839

still remain challenging, and the precise adjustment of the elemental ratio is the key to the electrocatalytic activity.

Herein, we report a facile two-step solvothermal process to achieve the well-defined trimetallic CoNiFe sulfide mesoporous nanospheres (CoNiFe-S MNs), which we testified universality in other systems. Metal–organic frameworks (MOFs) were chosen as precursors owing to the enriched porous structures and highly controllable composition.<sup>[17]</sup> Driven by electrocatalytic functionality, we intentionally selected the optimized Fe, Co, and Ni ratio to realize the enhanced performance. The easily achieved MNs show high surface area and pore volume, which verifies the correctness of our proposal. Comparative tests and different characterizations of CoNiFe-S MNs and monometallic MNs indicate that the synergistic effect of trimetallic ions affects the electronic structures, which evinces the improved electrochemical performance.<sup>[18,19]</sup> The as-prepared trimetallic electrocatalysts exhibit an extremely low overpotential of 199 mV at a current density of 10 mA cm<sup>-2</sup> toward OER in 1 M KOH, as well as a half-wave potential ( $E_{1/2}$ ) of 0.78 V toward ORR in 0.1 M KOH. Control experiments with bimetallic sulfides and trimetallic sulfides with various metal ratio were also performed to validate our devisal. Have proved the OER and ORR catalytic activity, the catalyst was fabricated as air electrode in rechargeable Zn–air battery and exhibit good charge–discharge performance and a high power density, which significantly exceed those of the state-of-the-art Pt/C-Ir/C counterpart. Impressively, the structural merits inherited from mesopores is presented in stability tests, while the performance remains almost constant during the potentiostatic OER test and galvanostatic charge–discharge cycle.

## 2. Results and Discussion

### 2.1. Synthesis and Characterizations

The overall synthetic process is illustrated in **Figure 1a**. The trimetallic MOF nanospheres (CoNiFe-BTC) are prepared via a solvothermal process with 1,3,5-benzenetricarboxylic acid ( $H_3$ BTC) as organic linker. Fundamentally, the ratio of Fe, Co, and Ni ions will exert a significant influence on the electrochemical performance of trimetallic sulfides. Smith et al. reported the correlation of OER catalytic performance and the stoichiometry in amorphous metal oxide films containing Fe, Co, and Ni.<sup>[18]</sup> Based on their summarized contour plots, we selected a 2:5:5 ratio of Fe, Co, and Ni as the adding amount of corresponding metal salts. Field-emission scanning electron microscopy (FESEM) and transmission electron microscopy (TEM) images (**Figure S1a,b**, Supporting Information) show that products are monodispersed nanospheres with a uniform diameter of around 250 nm. X-ray diffraction (XRD) pattern (**Figure S1c**, Supporting Information) does not provide well-defined peaks, indicating the amorphous nature of precursor. Fourier-transformed infrared resonance (FT-IR) spectrum (**Figure S1d**, Supporting Information) reveals the reduction of frequency shift of C=O stretching from 1722 cm<sup>-1</sup> for noncoordinated  $H_3$ BTC to 1615 cm<sup>-1</sup>, associated with previous reported result,<sup>[20]</sup> suggesting the coordination between metal ions and organic ligands. The energy dispersive X-ray spectroscopy (EDS)

result (**Figure S1e**, Supporting Information) demonstrates the ratio of Fe, Co, and Ni is about 2:5:5, which is consistent with the adding amounts of metal salts. CoNiFe-BTC nanospheres were then treated with TAA at 150 °C and after the reaction, precursors successfully transformed into sulfide MNs. FESEM and TEM images (**Figure 1b,c**) reveal that CoNiFe-S MNs are about 250 nm in diameter, which is in good accordance with MOF precursors. Magnified TEM image (**Figure 1d**) and high-angle annular dark-field scanning TEM (HAADF-STEM) image (**Figure 1e**) illustrate that nanosphere is assembled by small crystals. Elemental mapping images show that Fe, Co, Ni, and S are uniformly distributed throughout the MNs, with a little incorporation of O. The ratio of Fe, Co, and Ni is around 2:5:5 (**Figure S2**, Supporting Information), which is in good agreement with that of MOF precursor. High-resolution TEM (HRTEM) image (**Figure 1f**) and XRD pattern (**Figure 1g**) of MNs reveal that the structure is (Co,Ni)<sub>3</sub>S<sub>4</sub> (JCPDS No. 11-0068) and (Fe,Ni)<sub>3</sub>S<sub>4</sub> (JCPDS No. 11-0095), and the characteristic lattice fringe spacing of 0.235 and 0.286 nm could be well indexed to the interplanar spacing of (311) and (440) planes in (Co,Ni)<sub>3</sub>S<sub>4</sub> and (Fe,Ni)<sub>3</sub>S<sub>4</sub>, respectively. Considering that the (Co,Ni)<sub>3</sub>S<sub>4</sub> and (Fe,Ni)<sub>3</sub>S<sub>4</sub> both have the spinel structure, the trimetallic ions would be uniformly distributed in the octahedral and tetrahedral sites of fcc packed sulfur ions, for the trimetallic sulfides with different metal ratios have the almost same XRD patterns (**Figure S4**, Supporting Information). To further characterize the mesoporous structure, we studied the surface area as well as pore volume and distribution. **Figure 1h** displays the N<sub>2</sub> adsorption–desorption curve of CoNiFe-S MNs. Brunauer–Emmett–Teller (BET) surface area of MNs is calculated as 166.0 m<sup>2</sup> g<sup>-1</sup>. The N<sub>2</sub> adsorption–desorption curve can be identified as type IV isotherm, which indicates the existence of mesopores.<sup>[21]</sup> The as-prepared sulfide MNs also exhibit remarkable pore volume of 0.585 cm<sup>3</sup> g<sup>-1</sup>, characterized by Barrett–Joyner–Halenda (BJH) method. The BJH pore-size distribution curve (the inset of **Figure 1h**) manifests that the dominant distribution of pores lies in around 2.4, 3.8, and 16.1 nm. The formation mechanism of CoNiFe-S MNs was inferred to be an ion-exchange process according to time-dependent TEM images and XRD patterns (**Figures S5 and S6**, Supporting Information), which is discussed in the Supporting Information in detail.

With the successful achievement of CoNiFe-S MNs, we not only expanded the method to bimetallic and monometallic systems, but also achieved different morphologies to confirm the versatility of the strategy. First, we explored bimetallic and unary systems. **Figure 2a** displays TEM image of CoNi-S MNs. The products are uniform nanospheres, while the sizes are consistent with CoNi-BTC precursors (**Figure S7**, Supporting Information). The mesoporous morphology is similar with that of CoNiFe-S MNs. HAADF-STEM images and EDS elemental mapping images (**Figure 2b,c**) reveal that CoNi-S MNs are also assembled by small nanocrystals and the elements uniformly distribute in the nanospheres. Characterized by XRD (**Figure S12a**, Supporting Information), the chemical component of CoNi-S MNs is NiCo<sub>2</sub>S<sub>4</sub> (JCPDS No. 43-1477). CoNi-S with other metal ratios could also be prepared and the close XRD patterns indicate that the structure could all be denoted as (Co,Ni)<sub>3</sub>S<sub>4</sub> (**Figure S13**, Supporting Information). CoFe-S,



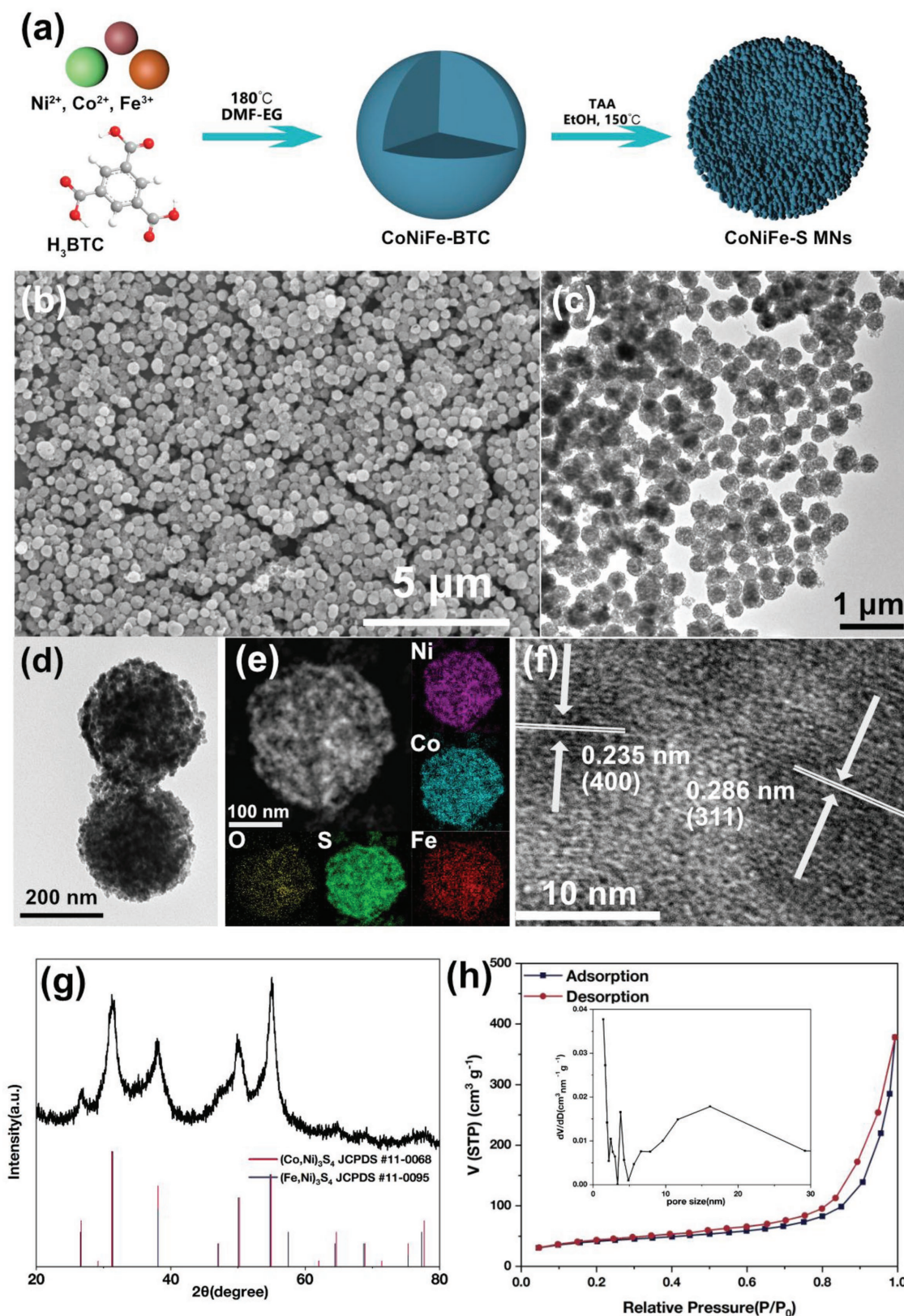


**Figure 1.** a) Schematic illustration of synthetic route of CoNiFe-S MNs. Structural characterization of CoNiFe sulfide MNs: b) FESEM, c) TEM and d) enlarged TEM images, e) HAADF-STEM and elemental mapping images, f) HRTEM images, g) XRD pattern with the standard patterns for  $\text{NiCo}_2\text{S}_4$  and  $\text{FeNi}_2\text{S}_4$ , and h) nitrogen adsorption and desorption isotherms measured at 77 K. Inset: the corresponding pore size distribution.

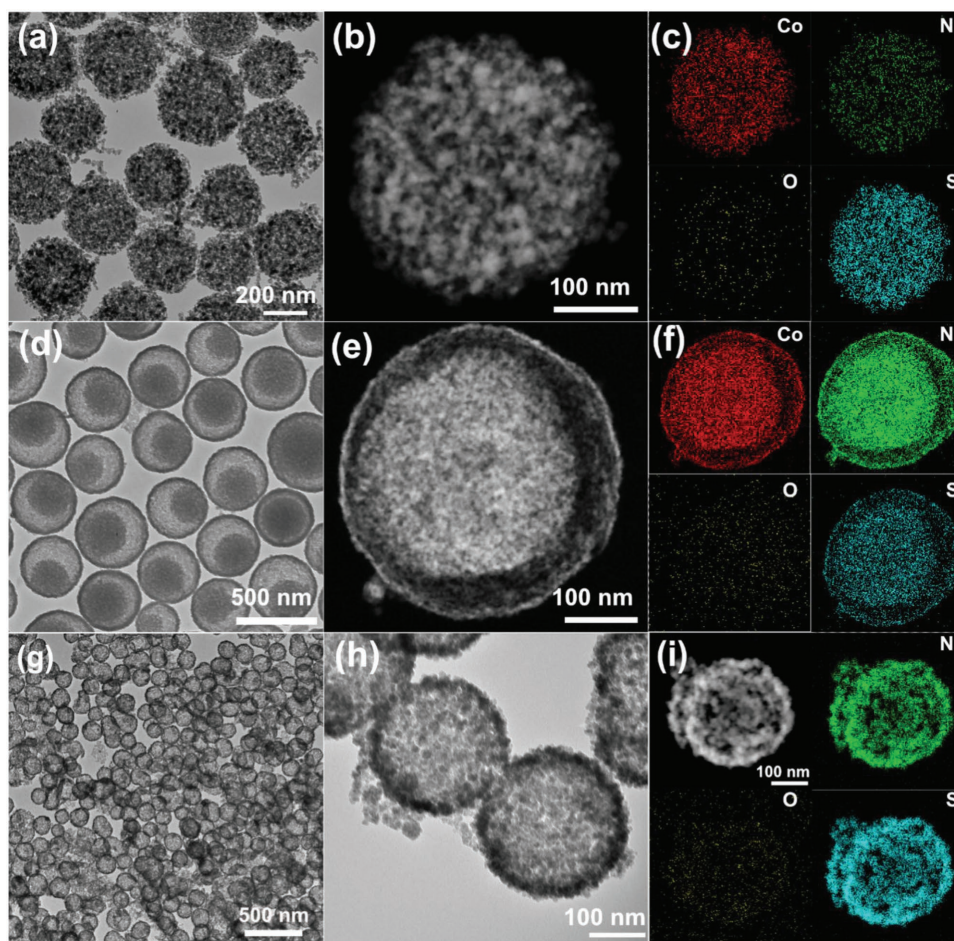


**Figure 2.** Methodological expansion for bimetallic and monometallic systems. a–c) TEM image, HAADF-STEM image and elemental mapping images of CoNi-S MNs, d–f) TEM image, HAADF-STEM image, and elemental mapping images of CoNi-S yolk-shell nanospheres, g–i) normal and enlarged TEM images, HAADF-STEM image, and elemental mapping images of Ni-S hollow nanospheres.

NiFe-S MNs, and Co-S MNs could also be prepared analogously with similar mesoporous morphology (Figures S14 and S15, Supporting Information).

Aside from mesoporous morphology, other novel structures could also be achieved with different methodological modification. By decreasing the concentration of precursor and TAA, the yolk-shell CoNi-S nanospheres could be achieved.<sup>[22]</sup> TEM and HAADF-STEM images (Figure 2d,e) exhibits that the inner core of yolk-shell NiCo<sub>2</sub>S<sub>4</sub> structure has similar mesoporous structure but encapsulated within a shell. Elemental mapping images (Figure 2f) display the uniform distribution of all elements in shell and yolk areas. As for unary Ni sulfide, a well-defined hollow nanospheres could be obtained (Figure 2g). Enlarged TEM images (Figure 2h) reveals that the Ni-S has similar crystals-assembled structure, while the interior becomes hollower than mesoporous analogs. Fe sulfide is a little morphologically different (Figure S16, Supporting Information). The small crystals incorporated with nanosheets should be ascribed to the 3D gel-like Fe-BTC precursors (Figure S11, Supporting Information). It is fascinating to further discovery the reaction mechanisms of these different structures, and further work may be presented elsewhere.

To disclose the electronic states of CoNiFe-S MNs, we studied high-resolution X-ray photoelectron spectroscopy (XPS) spectra and made comparisons with monometallic sulfides. According to the Co 2p spectrum of CoNiFe-S MNs (Figure 3a), the peaks located at 778.5 and 793.4 eV are corresponding to 2p<sub>3/2</sub> and 2p<sub>1/2</sub> orbitals of Co-S,<sup>[12,23,24]</sup> and peaks located at 779.6 and 794.7 eV are corresponding to 2p<sub>3/2</sub> and 2p<sub>1/2</sub> orbitals of Co<sup>3+</sup>, while the peak at 781.9 and 798.1 eV should be attributed to Co<sup>2+</sup>.<sup>[25]</sup> Compared with unary sulfide, the Co 2p peaks shift downward to lower binding energy, implying the electron rich state. Similarly, in Ni 2p spectra (Figure 3b), the peaks at 853.2 and 870.5 eV are assigned to 2p<sub>3/2</sub> and 2p<sub>1/2</sub> orbitals of Ni-S, and peaks at 855.5 and 873.4 eV are associated with 2p<sub>3/2</sub> and 2p<sub>1/2</sub> orbitals of Ni<sup>3+</sup>.<sup>[26]</sup> Compared with monometallic sulfide, the Ni 2p peaks also exhibit a slightly negative shift, indicating the existence of electron acceptance.<sup>[27]</sup> As for Fe 2p spectrum (Figure 3c), the peaks at 706.6 and 720.1 eV are comparable to literature value of Fe-S,<sup>[28]</sup> and the peaks at around 711.9 and 724.8 eV indicate the existence of Fe<sup>3+</sup>.<sup>[29]</sup> The peak at higher binding energy of 714.6 eV could be assigned to high valence species.<sup>[27]</sup> Varied from Co and Ni 2p spectra, Fe 2p<sub>3/2</sub> peaks significantly shift to higher binding energy compared to



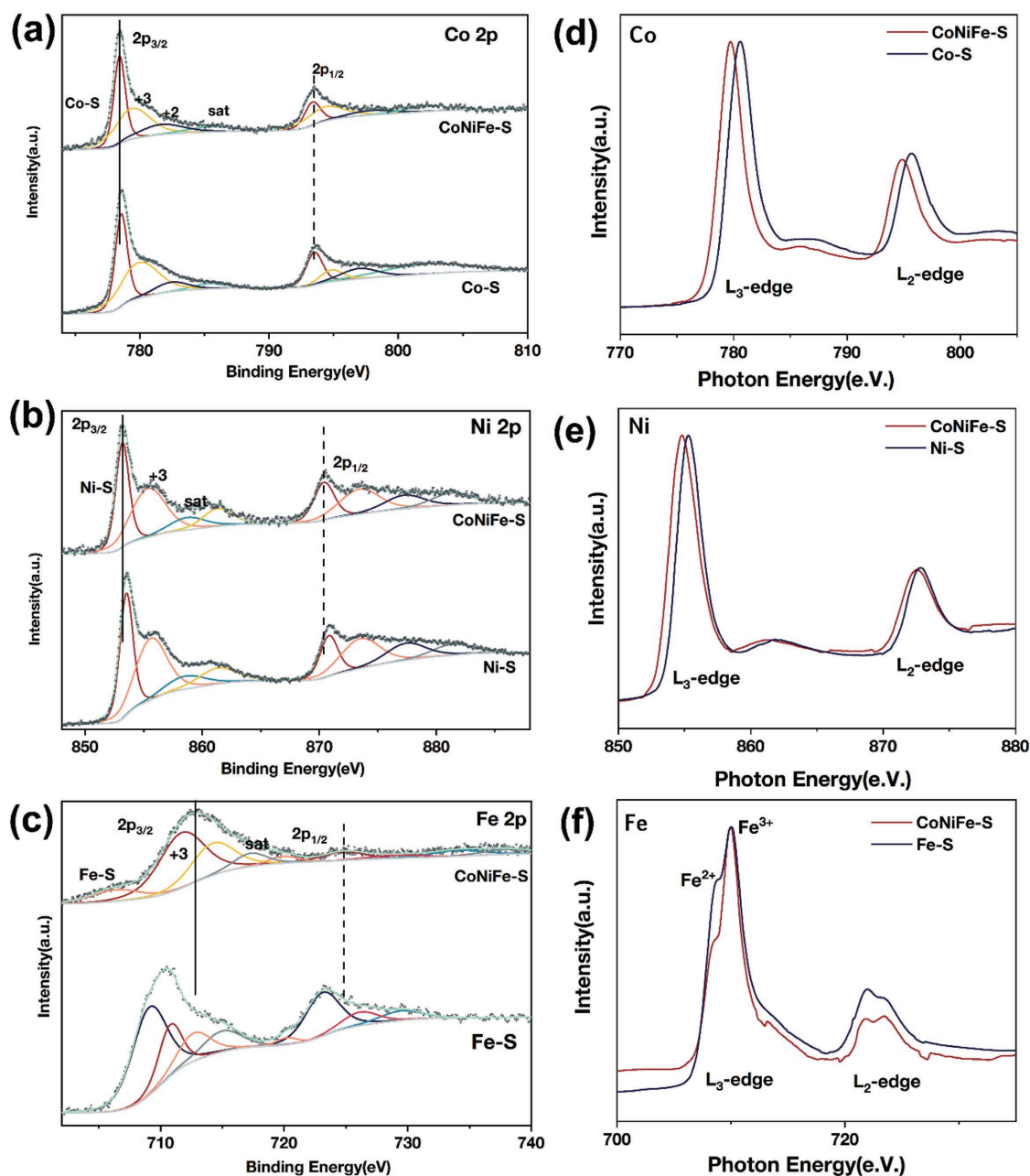


**Figure 3.** High-resolution XPS spectra of trimetallic and monometallic sulfides. For a) Co 2p, b) Ni 2p, and c) Fe 2p regions. Normalized d) Co, e) Ni, f) Fe L-edge sXAS spectra of CoNiFe-S MNs and monometallic sulfides using TEY method.

unary iron sulfide, suggesting more electron positive nature of Fe in the CoNiFe-S MNs. The peak shifts in Co, Ni, and Fe spectra imply that the incorporated Fe would serve as electronic modulator, to provide more electron to Co and Ni, increasing the electron density of these active sites and weakening the metal–O bond, which would be beneficial to the oxygen-involved electrocatalysis.<sup>[12,27]</sup> This phenomenon is consistent with previous report that the addition of Fe would reduce the average oxidation state of Ni, which could be beneficial to the electrocatalysis.<sup>[30]</sup> Additionally, the high valance Fe species could also serve as OER active center.<sup>[31]</sup> Besides, the integration of Co, Ni, and Fe also modulate the chemical state of sulfur. As

can be seen in Figure S17 of the Supporting Information, compared with unary metal sulfides, the S 2p spectrum of CoNiFe-S MNs slightly shifts to higher binding energy, manifesting the decreased electronic density of S. In summary, the synergistic effect of trimetallic ions could tailor the electronic structure and will be beneficial to the oxygen-involved electrocatalysis.

In order to delve deeply into the synergistic effect of trimetallic ions, as well as validate XPS results, we used synchrotron-based soft X-ray adsorption spectroscopy (sXAS) to investigate the electron states.<sup>[32]</sup> The sXAS spectra were obtained in the total electron yield (TEY) mode. As can be seen from Figure 3d,e, the peaks of Co and Ni L<sub>3</sub>-edge both shift to lower energy, indicating

the lower average oxidation state, which is identical with previous XPS analysis. As for Fe  $L_{3}$ -edge (Figure 3f), the proportion of  $Fe^{3+}$  significantly increases compared to monometallic Fe-S.<sup>[33]</sup> So it can be concluded that the incorporation of Fe will serve as electron donor to reduce the oxidation states of Co and Ni, which would be favorable to electrocatalysis process.

## 2.2. Electrochemical Performance

To finally verify the superiority of the trimetallic sulfides, we first investigated the OER performance of as-synthesized samples. The electrocatalysts are loaded on carbon fiber paper (CFP) as working electrode. The measurements were performed in 1 M KOH solution using a typical three-electrode system, and polarization curves were recorded with  $iR$ -compensation. Monometallic sulfides and CoNiFe-S solid nanospheres (SNs) (Figure S18, Supporting Information) are used as referential materials. **Figure 4a** shows the linear scanning voltammogram (LSV). CoNiFe-S MNs perform the lowest overpotential of only 199 mV at a current density of  $10 \text{ mA cm}^{-2}$ , which has the notable differences of 73, 81, and 95 mV lower than that of Co-S, Ni-S, and Fe-S, respectively. The CoNiFe-S SNs exhibit similar overpotential at low current density, implying the similar chemical states of the two kinds of trimetallic sulfides. However, the current increasing trend of SNs is significantly lower than trimetallic sulfide MNs and even other MNs, which proves that mesopores are beneficial for further current increase due to the improved gas transport and exposure of active sites. The OER kinetics were revealed by Tafel plot (Figure 4b).<sup>[34]</sup> Tafel slope of CoNiFe-S, Co-S, Ni-S, and Fe-S are 50.1, 70.0, 90.9, and 59.6  $\text{mV dec}^{-1}$ , respectively. The relatively lower Tafel slope manifests that the trimetallic sulfide MNs would provide a higher intrinsic activity. The electrochemical active surface area is roughly estimated by electrochemical double-layer capacitance ( $C_{dl}$ ). Figure S21a of the Supporting Information plots the  $C_{dl}$  of different materials, and it can be seen that all sulfide MNs possess larger  $C_{dl}$  than Ni-S hollow nanospheres and the Fe-S sample. Especially, the CoNiFe-S nanospheres present the largest  $C_{dl}$ , and MNs show larger  $C_{dl}$  than SNs, demonstrating that both mesoporous structure and integration of trimetallic ions contribute to the large catalytically active surface area, which is advantageous to the exposure of active sites and greatly contributes the superior OER performance.<sup>[34,35]</sup> Aside from as-mentioned tests, we compared performance of trimetallic and bimetallic sulfide MNs. According to Figure S22 of the Supporting Information, the CoNiFe-S MNs exhibit lower overpotential at current density of  $10 \text{ mA cm}^{-2}$  and Tafel slope than CoNi-S MNs, CoFe-S MNs, and NiFe-S MNs, indicating the compositional advantage of trimetallic ions, which further confirm our hypothesis that Fe can modulates the electron structures of Co and Ni, and the three metal ions are all beneficial to the OER electrocatalytic activity.

Different stability tests were also carried out to investigate the durability of the catalysts. First, a chronoamperometry method with a fixed overpotential of 310 mV was implemented. The current density remains almost unchanged after 50 h running, illustrated in Figure 4c. The fluctuation of the curve could be ascribed to the corrosion of CFP. We also used a

galvanic pulse method to study the inherent structural stability under large alternating current. Two constant current density of 40 and  $80 \text{ mA cm}^{-2}$  were set with an iteration period of 1 h. As shown in Figure S23 of the Supporting Information, the potential increases quite little after 24 h, demonstrating the good structural recoverability of CoNiFe-S MNs. The excellent stability demonstrates the inherent structural advantages of the mesoporous morphology, which could provide a rapid release of produced oxygen bubbles and enable the continuously exposure of inner active sites.

To prove the Faradaic efficiency of water oxidation, the rotating ring disk electrode (RRDE) technique was employed.<sup>[36,37]</sup> The plots of ring current, disk current, and Faradaic efficiency versus the potential applied to the disk electrode are displayed in Figure 4d. The electrocatalyst shows a high efficiency of around 99.2% at the first potential of 1.420 V, and the following decrease of Faradaic efficiency result from the large amount of undissolved  $O_2$  bubbles generated from relatively higher potential which cannot be fully reduced by Pt ring electrode.<sup>[37]</sup>

Finally, catalysts collected after CP tests were characterized to check the structure and morphology changes. As shown in Figure S25 of the Supporting Information, the TEM image reveals that the mesoporous morphology maintained after the OER catalysis. XPS spectra of samples collected after both CP and cyclic voltammetry tests manifest that all Co, Ni, and Fe 2p peaks shift to higher binding energy and the metal-S peaks vanished, demonstrating the oxidation of the sulfides and formation of oxides or (oxy)hydroxides. The S 2p peaks also weaken and the peak located at 168.5 eV which corresponds to sulfate species significantly enhanced,<sup>[13]</sup> suggesting the substitution of S by O. Elemental mapping images also evidence the fact that S is replaced by O during the OER catalysis. It can be inferred that metal hydroxides is major active center and the existence of sulfide will improve the activity.<sup>[14,24]</sup>

After evaluating the excellent OER activity, we further studied the ORR catalytic performance to demonstrate the bifunctionality. The catalyst exhibits a half-wave potential ( $E_{1/2}$ ) of 0.78 V in 0.1 M KOH (**Figure 5e**), which is close with commercial Pt/C (0.842 V). The CoNiFe-S MNs also show comparable diffusion-limited current density at negative potential compared with Pt/C. Additionally, Koutecky–Levich (K–L) plot is used for investigating the kinetics of ORR. As shown in inset of Figure 5f, the electron-transfer number ( $n$ ) of CoNiFe-S MNs is from 3.86 to 3.97 at different potentials for 0.2 to 0.3 V versus RHE, which confirms the dominant four-electron transfer process.<sup>[38]</sup> The structural recoverability is corroborated by ORR stability test again, and Figure S26c of the Supporting Information displays that the trimetallic sulfide exhibits much better durability than commercial Pt/C, with around 12% drop of current density after the 10 h potentiostatic run, as comparison, that of Pt/C decrease by  $\approx 45\%$ . Since the value between the potential with a current density of  $10 \text{ mA cm}^{-2}$  for OER ( $E_{j=10}$ ) and the half-wave potential ( $E_{1/2}$ ) for ORR is broadly regarded as an assessment for the bifunctional OER and ORR activity, the overall ORR and OER test was recorded in 0.1 M KOH. According to Figure S26a of the Supporting Information, the potential difference ( $\Delta E$ ) is only 0.71 V, which is markedly lower than that of Pt/C (0.88 V), and it is obvious that the low OER overpotential

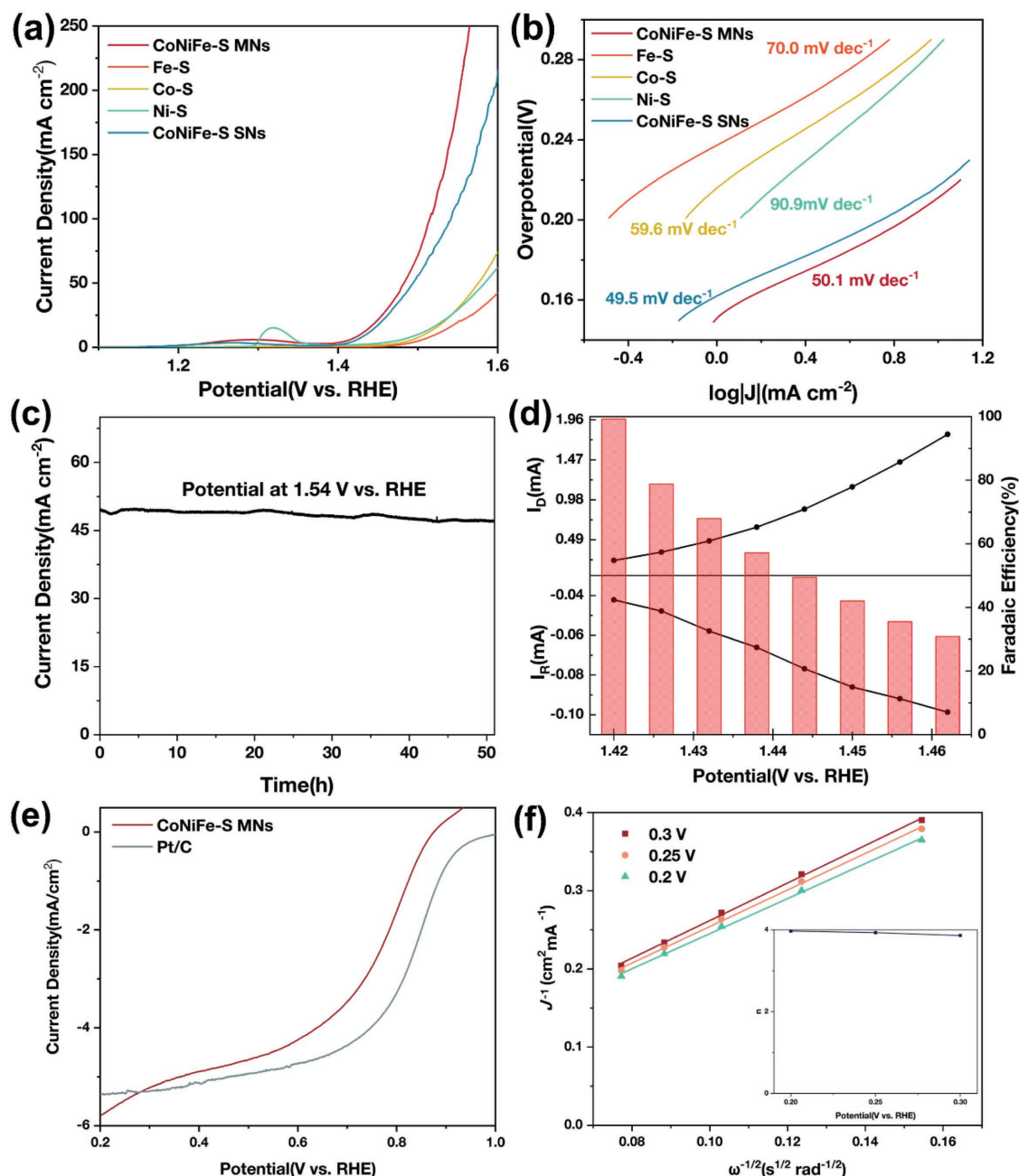


**Figure 4.** OER and ORR electrocatalytic characterizations. a) LSV curves recorded with 95%  $iR$ -compensation, b) Tafel plots, c) chronoamperometric response ( $i-t$ ) recorded on CoNiFe-S MNs for 50 h at constant potential of 1.54 V versus RHE, d) Faradaic efficiency measurement of the CoNiFe-S MNs in 1 M KOH at a rotating rate of 1600 rpm under a nitrogen atmosphere. The disk and ring currents and the Faradaic efficiency of RRDE are plotted as a function of the applied disk potential. The ring potential is fixed at 0.32 V versus RHE. ORR electrocatalytic characterizations. e) polarization curves, f) the Koutecky–Levich (K–L) plots. Inset: the electron transfer number of the CoNiFe-S MNs.

considerably contribute to the low  $\Delta E$ . The good ORR catalytic activity additionally proves our perspectives on design high-performance bifunctional electrocatalysts for Zn–air batteries. In order to verify our selection on the metal ratio, additional control electrocatalytic tests of trimetallic sulfides with different stoichiometry of Fe, Co, and Ni were carried out. According to Figures S27 and S28, Tables S2 and S3 of the Supporting Information, the sulfide with Fe, Co, and Ni ratio of 2:5:5 evince the best OER performance in both 1 and 0.1 M KOH, and show

the lowest  $\Delta E$  in 0.1 M KOH. The experimental results prove correctness of our selection of 5:5:2 ratio of Co, Ni, and Fe.

Finally, we assembled the rechargeable Zn–air battery to explore the accessibility of CoNiFe-S MNs in fabricating practical device. The electrolyte is the mixed solution of 6 M KOH and 0.2 M  $ZnCl_2$ , and the catalyst is loaded on carbon cloth as air electrode, while Zn foil serves as anode, as illustrated in Figure 5a. The 1:1 mixture of Pt/C and Ir/C was selected as reference. The charge and discharge curves are displayed in



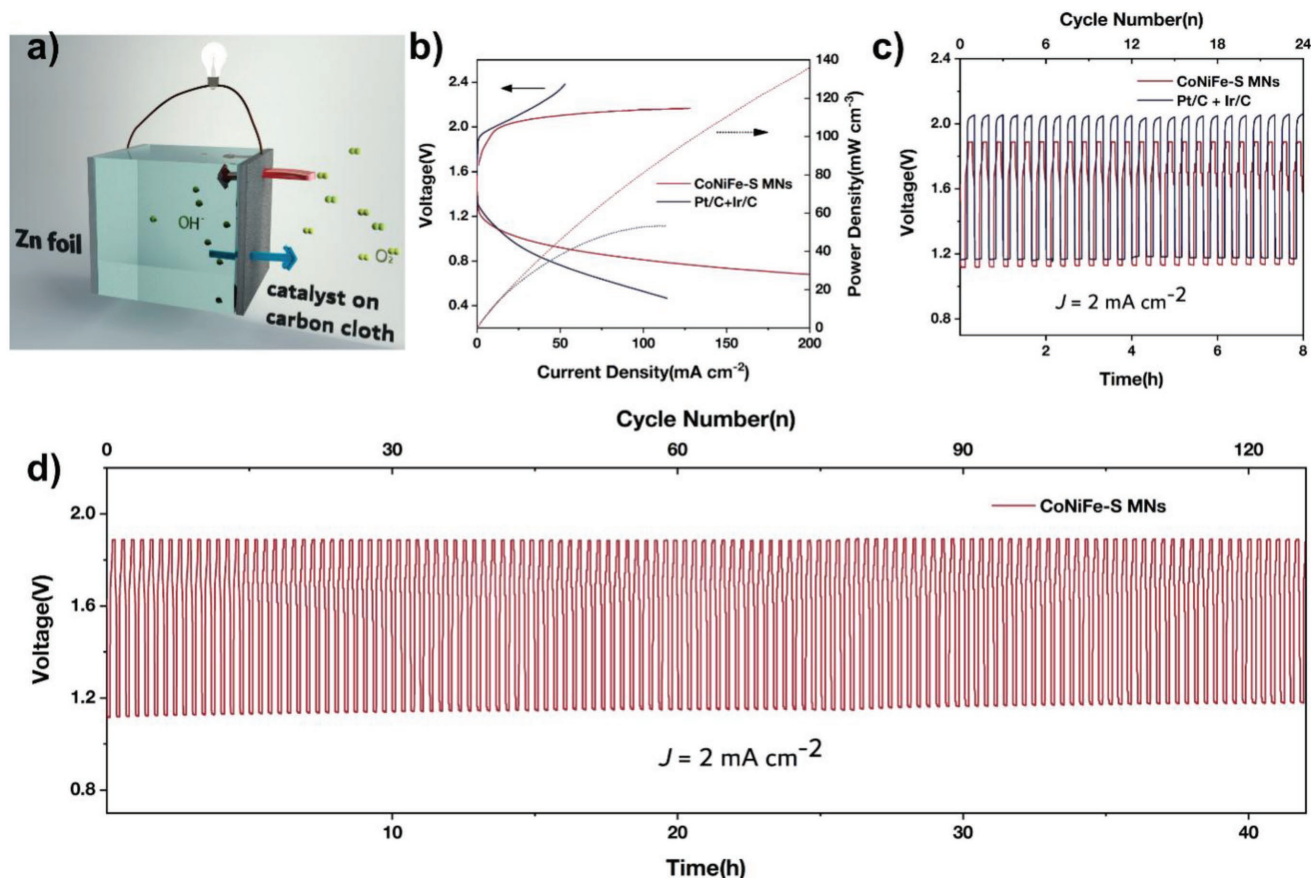


**Figure 5.** a) Schematic illustration of Zn-air battery. b) Galvanodynamic charge and discharge and power density curves for CoNiFe-S MNs and Pt/C + Ir/C. c) Galvanostatic charge-discharge cycling curves of CoNiFe-S MNs and Pt/C + Ir/C at the current density of  $2.0 \text{ mA cm}^{-2}$ . d) Long-time cycling curve of Zn-air battery with CoNiFe-S MNs as air electrode catalyst.

Figure 5b. According to the plot, the CoNiFe-S MNs show much better performance than the Pt/C-Ir/C couple, achieving a voltage of 0.92 and 2.10 V at the charge and discharge current densities of  $50 \text{ mA cm}^{-2}$ . As comparison, the Pt/C-Ir/C presents the corresponding value of 0.76 and 2.34 V, respectively. Moreover, the maximum power density of CoNiFe-S MNs approaches  $140 \text{ mW cm}^{-2}$ , which substantially outperforms the Pt/C-Ir/C couple reference. The galvanostatic charge and discharge curves were also recorded. As can be seen from Figure 5c, the CoNiFe-S MNs show a low charge-discharge voltage gap of 0.76 V, with a decrease by around 16% compared with that of Pt/C-Ir/C couple (0.91 V), and this result is consistent with previous  $\Delta E$  data. The structural advantage of mesoporous feature is further evidenced by the long-term charge-discharge cycling test. The sample maintains a voltage gap of 0.74 V after more than 40 h/120 cycles durability test. The excellent performance and durability all evince the structural and compositional advantages of the nanomaterials and further confirm our proposal of multimetal integration.

### 3. Conclusion

In summary, we have successfully achieved well-defined trimetallic CoNiFe sulfide MNs through an anion-exchange

method using MOF precursor and thioacetamide. The synthetic procedure can be expanded to monometallic and bimetallic system with many derivatives. Moreover, the spectroscopic characterizations reveal the synergistic effect of trimetallic ions, which would be promising for OER and ORR electrocatalysis. The subsequent electrochemical tests provide the verification. The trimetallic sulfide MNs exhibit enhanced OER performance with an overpotential of only 199 mV at current density of  $10 \text{ mA cm}^{-2}$  and a small Tafel slope of  $50.1 \text{ mV dec}^{-1}$ , as well as long-term stability performance. Control experiments with monometallic, bimetallic sulfides, and trimetallic sulfides with different elemental ratios supported our devisal and spectroscopic analysis result. Aside from excellent OER performance, the catalyst also exhibit a half-wave potential of 0.78 V in ORR assessment, and a potential gap of 0.71 V between  $E_{1/10}$  and  $E_{1/2}$  compared with that of 0.88 V of Pt/C. Finally, as a practical application, a rechargeable Zn-air battery is assembled to affirm the high activity. The CoNiFe-S MNs present remarkable charge-discharge and long-term cycle performance. We believe this method could be further extended to many other MOF systems to develop novel mesoporous materials and self-standing materials, and will be attractive for the design of high performance electrocatalysts, other energy-related applications and for fabrication of devices.

## Supporting Information

Supporting Information is available from the Wiley Online Library or from the author.

## Acknowledgements

This work was supported by National Key R&D Program of China (2017YFA0700101 and 2016YFA0202801), and the NSFC (21431003 and 21521091).

## Conflict of Interest

The authors declare no conflict of interest.

## Keywords

electrocatalysis, mesoporous materials, sulfides, trimetallic ions, Zn–air batteries

Received: June 13, 2018  
Revised: September 21, 2018  
Published online: October 15, 2018

- [1] S. Chu, Y. Cui, N. Liu, *Nat. Mater.* **2017**, *16*, 16.
- [2] a) F. Cheng, J. Chen, *Chem. Soc. Rev.* **2012**, *41*, 2172; b) J. Fu, Z. P. Cano, M. G. Park, A. Yu, M. Fowler, Z. Chen, *Adv. Mater.* **2017**, *29*, 1604685.
- [3] a) Y. Li, J. Lu, *ACS Energy Lett.* **2017**, *2*, 1370; b) Y. Li, H. Dai, *Chem. Soc. Rev.* **2014**, *43*, 5257.
- [4] I. Katsounaros, S. Cherevko, A. R. Zeradjanin, K. J. J. Mayrhofer, *Angew. Chem., Int. Ed.* **2014**, *53*, 102.
- [5] Z. W. Seh, J. Kibsgaard, C. F. Dickens, I. Chorkendorff, J. K. Nørskov, T. F. Jaramillo, *Science* **2017**, *355*, eaad4998.
- [6] a) Z. F. Huang, J. Wang, Y. Peng, C. Y. Jung, A. Fisher, X. Wang, *Adv. Energy Mater.* **2017**, *7*, 1700544; b) M. Kuang, G. Zheng, *Small* **2016**, *12*, 5656.
- [7] a) C. Hu, L. Zhang, Z. J. Zhao, J. Luo, J. Shi, Z. Huang, J. Gong, *Adv. Mater.* **2017**, *29*, 1701820; b) F. Meng, H. Zhong, D. Bao, J. Yan, X. Zhang, *J. Am. Chem. Soc.* **2016**, *138*, 10226; c) S. Chen, Z. Kang, X. Hu, X. Zhang, H. Wang, J. Xie, X. Zheng, W. Yan, B. Pan, Y. Xie, *Adv. Mater.* **2017**, *29*, 1701687.
- [8] M. H. Sun, S. Z. Huang, L. H. Chen, Y. Li, X. Y. Yang, Z. Y. Yuan, B. L. Su, *Chem. Soc. Rev.* **2016**, *45*, 3479.
- [9] a) H.-W. Liang, X. Zhuang, S. Brüller, X. Feng, K. Müllen, *Nat. Commun.* **2014**, *5*, 4973; b) X. Zhang, S. Liu, Y. Zang, R. Liu, G. Liu, G. Wang, Y. Zhang, H. Zhang, H. Zhao, *Nano Energy* **2016**, *30*, 93.
- [10] a) W. Li, J. Liu, D. Zhao, *Nat. Rev. Mater.* **2016**, *1*, 16023; b) Q. Wei, F. Xiong, S. Tan, L. Huang, E. H. Lan, B. Dunn, L. Mai, *Adv. Mater.* **2017**, *29*, 1602300.
- [11] a) L. Han, S. Dong, E. Wang, *Adv. Mater.* **2016**, *28*, 9266; b) H. Li, S. Chen, X. Jia, B. Xu, H. Lin, H. Yang, L. Song, X. Wang, *Nat. Commun.* **2017**, *8*, 15377; c) S. Zhao, Y. Wang, J. Dong, C.-T. He, H. Yin, P. An, K. Zhao, X. Zhang, C. Gao, L. Zhang, J. Lv, J. Wang, J. Zhang, A. M. Khattak, N. A. Khan, Z. Wei, J. Zhang, S. Liu, H. Zhao, Z. Tang, *Nat. Energy* **2016**, *1*, 16184.
- [12] H.-F. Wang, C. Tang, B. Wang, B.-Q. Li, Q. Zhang, *Adv. Mater.* **2017**, *29*, 1702327.
- [13] P. Cai, J. Huang, J. Chen, Z. Wen, *Angew. Chem., Int. Ed.* **2017**, *56*, 4858.
- [14] B. Ni, T. He, J.-o. Wang, S. Zhang, C. Ouyang, Y. Long, J. Zhuang, X. Wang, *Chem. Sci.* **2018**, *9*, 2762.
- [15] a) H. Li, S. Chen, Y. Zhang, Q. Zhang, X. Jia, Q. Zhang, L. Gu, X. Sun, L. Song, X. Wang, *Nat. Commun.* **2018**, *9*, 2452; b) Q. L. Zhu, W. Xia, T. Akita, R. Zou, Q. Xu, *Adv. Mater.* **2016**, *28*, 6391.
- [16] a) J. Staszak-Jirkovsky, C. D. Malliakas, P. P. Lopes, N. Danilovic, S. S. Kota, K. C. Chang, B. Genorio, D. Strmcnik, V. R. Stamenkovic, M. G. Kanatzidis, N. M. Markovic, *Nat. Mater.* **2016**, *15*, 197; b) X. Long, G. Li, Z. Wang, H. Zhu, T. Zhang, S. Xiao, W. Guo, S. Yang, *J. Am. Chem. Soc.* **2015**, *137*, 11900.
- [17] a) S. Dang, Q.-L. Zhu, Q. Xu, *Nat. Rev. Mater.* **2017**, *3*, 17075; b) X. Cao, C. Tan, M. Sindoro, H. Zhang, *Chem. Soc. Rev.* **2017**, *46*, 2660; c) H. Yang, X. Wang, *Adv. Mater.* **2018**, *1800743*, <https://doi.org/10.1002/adma.201800743>.
- [18] R. D. Smith, M. S. Prevot, R. D. Fagan, S. Trudel, C. P. Berlinguette, *J. Am. Chem. Soc.* **2013**, *135*, 11580.
- [19] D. Friebe, M. W. Louie, M. Bajdich, K. E. Sanwald, Y. Cai, A. M. Wise, M. J. Cheng, D. Sokaras, T. C. Weng, R. Alonso-Mori, R. C. Davis, J. R. Bargar, J. K. Nørskov, A. Nilsson, A. T. Bell, *J. Am. Chem. Soc.* **2015**, *137*, 1305.
- [20] X. Xu, S. Chen, Y. Chen, H. Sun, L. Song, W. He, X. Wang, *Small* **2016**, *12*, 2982.
- [21] D. P. Serrano, J. Aguado, J. M. Escola, J. M. Rodríguez, Á. Peral, *Chem. Mater.* **2006**, *18*, 2462.
- [22] L. Shen, L. Yu, H. B. Wu, X. Y. Yu, X. Zhang, X. W. Lou, *Nat. Commun.* **2015**, *6*, 6694.
- [23] M. S. Faber, R. Dziedzic, M. A. Lukowski, N. S. Kaiser, Q. Ding, S. Jin, *J. Am. Chem. Soc.* **2014**, *136*, 10053.
- [24] W. Chen, H. Wang, Y. Li, Y. Liu, J. Sun, S. Lee, J. S. Lee, Y. Cui, *ACS Cent. Sci.* **2015**, *1*, 244.
- [25] a) L. Xu, Q. Jiang, Z. Xiao, X. Li, J. Huo, S. Wang, L. Dai, *Angew. Chem., Int. Ed.* **2016**, *55*, 5277; b) P. Sennu, M. Christy, V. Aravindan, Y.-G. Lee, K. S. Nahm, Y.-S. Lee, *Chem. Mater.* **2015**, *27*, 5726.
- [26] H. Liang, F. Meng, M. Caban-Acevedo, L. Li, A. Forticaux, L. Xiu, Z. Wang, S. Jin, *Nano Lett.* **2015**, *15*, 1421.
- [27] Y. Xin, X. Kan, L. Y. Gan, Z. Zhang, *ACS Nano* **2017**, *11*, 10303.
- [28] S. Shukla, N. H. Loc, P. P. Boix, T. M. Koh, R. R. Prabhakar, H. K. Mulmudi, J. Zhang, S. Chen, C. F. Ng, C. H. A. Huan, N. Mathews, T. Sritharan, Q. Xiong, *ACS Nano* **2014**, *8*, 10597.
- [29] T. Yamashita, P. Hayes, *Appl. Surf. Sci.* **2008**, *254*, 2441.
- [30] M. W. Louie, A. T. Bell, *J. Am. Chem. Soc.* **2013**, *135*, 12329.
- [31] a) J. Y. C. Chen, L. Dang, H. Liang, W. Bi, J. B. Gerken, S. Jin, E. E. Alp, S. S. Stahl, *J. Am. Chem. Soc.* **2015**, *137*, 15090; b) H. Xiao, H. Shin, W. A. Goddard, *Proc. Natl. Acad. Sci. USA* **2018**, *115*, 5872.
- [32] a) F. Lin, Y. Liu, X. Yu, L. Cheng, A. Singer, O. G. Shpyrko, H. L. Xin, N. Tamura, C. Tian, T. C. Weng, X. Q. Yang, Y. S. Meng, D. Nordlund, W. Yang, M. M. Doeff, *Chem. Rev.* **2017**, *117*, 13123; b) X. Liu, W. Yang, Z. Liu, *Adv. Mater.* **2014**, *26*, 7710.
- [33] X. Liu, D. Wang, G. Liu, V. Srinivasan, Z. Liu, Z. Hussain, W. Yang, *Nat. Commun.* **2013**, *4*, 2568.
- [34] C. C. McCrory, S. Jung, J. C. Peters, T. F. Jaramillo, *J. Am. Chem. Soc.* **2013**, *135*, 16977.
- [35] T. Y. Ma, S. Dai, M. Jaroniec, S. Z. Qiao, *J. Am. Chem. Soc.* **2014**, *136*, 13925.
- [36] X. Yu, M. Zhang, W. Yuan, G. Shi, *J. Mater. Chem. A* **2015**, *3*, 6921.
- [37] A. T. Swesi, J. Masud, M. Nath, *Energy Environ. Sci.* **2016**, *9*, 1771.
- [38] Z. Miao, X. Wang, M.-C. Tsai, Q. Jin, J. Liang, F. Ma, T. Wang, S. Zheng, B.-J. Hwang, Y. Huang, S. Guo, Q. Li, *Adv. Energy Mater.* **2018**, *8*, 1801226.